The Astrophysical Journal Letters, 879:L22 (7pp), 2019 July 10 https://doi.org/10.3847/2041-8213/ab288e

Analysis of Jupiter's Deep Jets Combining *Juno* Gravity and Time-varying Magnetic Field Measurements

Keren Duer, Eli Galanti, and Yohai Kaspi
Department of Earth and Planetary Sciences, Weizmann Institute of Science, 234 Herzl st., 76100, Rehovot, Israel; keren.duer@weizmann.ac.il, kerenduer89@gmail.com
Received 2019 February 22; revised 2019 May 1; accepted 2019 June 10; published 2019 July 10

Abstract

Jupiter's internal flow structure is still not fully known, but can be now better constrained due to *Juno*'s high-precision measurements. The recently published gravity and magnetic field measurements have led to new information regarding the planet and its internal flows, and future magnetic measurements will help to solve this puzzle. In this study, we propose a new method to better constrain Jupiter's internal flow field using the *Juno* gravity measurements combined with the expected measurements of magnetic secular variation. Based on a combination of hydrodynamical and magnetic field considerations we show that an optimized vertical profile of the zonal flows that fits both measurements can be obtained. Incorporating the magnetic field effects on the flow better constrains the flow decay profile. This will get us closer to answering the persistent question regarding the depth and nature of the flows on Jupiter.

Key words: magnetohydrodynamics (MHD) – planets and satellites: atmospheres – planets and satellites: gaseous planets – planets and satellites: interiors – planets and satellites: magnetic fields

1. Introduction

The nature of Jupiter's interior is still a great mystery. The recent discovery that the depth of Jupiter's surface winds is ∼3000 km (Kaspi et al. 2018) raises the possibility that the flow penetrates to depths where the electrical conductivity is large enough so that the flow might interact with the magnetic field. Due to Jupiter's large mass and density, the inner pressure is high enough to cause gas ionization relatively close to its surface. Significant ionization is expected at ∼0.97 of the radius of Jupiter (∼2000 km from its surface), getting stronger with depth (Liu et al. 2008; French et al. 2012). According to the *Juno* gravity field measurements (Kaspi et al. 2018) the flow is expected to penetrate the ionized region and therefore influence the magnetic field and vice versa.

The electromagnetic (EM) induction equation describes the temporal variability of the magnetic field due to interaction with the flow, the strength of the magnetic field itself, and the electrical conductivity of the fluid. Because the electrical conductivity at Jupiter's higher atmosphere (cloud-level to ∼2000 km) is very low (Liu et al. 2008; French et al. 2012), the jet streams are expected to have no interaction with the magnetic field. In this region, the flows have a significant effect on the gravity field (Kaspi 2013; Kaspi et al. 2018). The inner region, below ∼2000 km with remnants of jet velocities, is associated with an electrical conductivity that increases exponentially with depth, and might affect magnetic field anomalies (Galanti et al. 2017a). Note that the transition between the two regions is likely gradual and not abrupt.

Several studies examined the possible interaction between the flow and the magnetic field in gas giants (e.g., Liu et al. 2008; Gastine & Wicht 2012; Jones 2014; Cao & Stevenson 2017; Dietrich & Jones 2018), but none have used the gravity and magnetic field measurements simultaneously to add constraints to the possible flow profile in Jupiter and other gaseous planets. Previous studies that estimated the flow decay structure have not considered the interaction between the flow and magnetic fields (e.g., Kaspi et al. 2018). One study presented the mean-field electrodynamic balance (MFED) as a method for constraining the deeper regions of the decay flow profile (Galanti et al. 2017a), but it is likely that due to the *Juno* measurements showing strong azimuthal variations in the magnetic field (Connerney et al. 2018), the magnetic field of Jupiter is too complicated for using the MFED method. Use of this method will result in a different vertical structure for each longitude, which is highly unconstrained. Conversely, the time changes in the magnetic field (also named magnetic secular variation) are likely to be measurable within the upcoming *Juno* measurements (Moore et al. 2018), and might be used to better constrain the flow field.

Temporal variation in the magnetic field generated by the core dynamo has been also identified for the Earth (e.g., Vestine & Kahle 1966; Kahle et al. 1967; Bloxham & Gubbins 1985), and estimated for other planetary interiors such as Jupiter's (e.g., Gastine et al. 2014; Jones 2014; Ridley & Holme 2016). On Earth, the secular variation (SV) is exploited to yield flow profiles at the top of Earth's outer core (Bloxham & Gubbins 1985; Bloxham 1992). While on Earth the SV strongly indicates internal flows in the core (Holme & Olson 2007), on Jupiter the SV can be a result of multiple origins, among them interior flows in the fully conductive region, external sources, and zonal flows in the semi-conductive region (Gastine et al. 2014; Ridley & Holme 2016). The SV timescale associated with zonal flows for Jupiter's magnetic field is estimated to be notable even within a single year (Gastine et al. 2014; Moore et al. 2018, 2019), if measured with high enough resolution. Moore et al. (2019) showed that time variations in Jupiter's internal magnetic field recorded from different spacecraft (from Pioneer 10 until *Juno*) over the past 50 yr are consistent with advection by zonal flows. However, since *Juno* revealed a complex longitudinal structured magnetic field, it is possible that using all passes of the *Juno* mission itself will allow us to track the advection of these longitudinal features and better estimate the vertical profile of the zonal flows.

In this study, we use the recently published gravity measurements from *Juno* (Iess et al. 2018), together with the

magnetic field measurements (Connerney et al. 2018) and the upcoming time-varying magnetic field measurements to better understand the nature of the deep flows in Jupiter. We present a method for the calculation of the decay profile of Jupiter's surface winds that can explain both the *Juno* gravity measurements and the time-varying magnetic measurements, which are currently measured by *Juno*. The latter are simulated and used to constrain the lower region of the flow decay profile by the EM induction equation that relates the magnetic secular variation to the flow strength. The upper region associated with strong flows is determined by relating the gravity field to the flows via thermal wind balance (Kaspi et al. 2010). We also characterize the transition between the regions using a variety of flow decay options and multiple transition options to find the best solution that can fit both measurements.

The manuscript is organized as follows: in Section 2 we present the relation connecting the flow field and the gravity (thermal wind (TW) balance), the magnetic secular variation (MSV) model, and describe the simulation and optimization processes. In Section 3 the combined solution based on both gravity and magnetic fields is presented, and in Section 4 we discuss the implications of this study and conclude.

2. Methodology

In order to better constrain the deep flow on Jupiter, we combine two fundamentally different approaches. The first is based purely on the gravity measurements and their relation to the flow via TW balance (e.g., Kaspi 2013; Galanti et al. 2017a; Kaspi et al. 2018), and the other is based on the EM induction equation called the MSV method (Bloxham & Gubbins 1985; Bloxham 1992). We aim to use the gravity constraints to find the best solution for the upper region of the flow, and the MSV method to better constrain the lower region of the flow and the transition between the regions.

2.1. Gravity Field Constraints

Jupiter's large size and rapid rotation imply that the leading-order momentum balance is geostrophic, namely a balance between the Coriolis force and the horizontal pressure gradients (Vallis 2006). Consequently, the leading-order vorticity balance is thermal wind balance (Kaspi et al. 2009). The zonal (azimuthal) component of the thermal wind balance is

$$2\Omega\frac{\partial}{\partial z}(\tilde{\rho}u) = \tilde{g}\frac{\partial \rho'}{\partial \theta}, \tag{1}$$

where Ω is the planetary rotation rate of Jupiter $\left(\frac{2\pi}{\Omega} \cong 9.92\ \mathrm{hr}\right)$, z is the direction parallel to the spin axis, $u(r, \theta)$ is the zonal flow, with θ being latitude and r is the depth, $\tilde{\rho}(r)$ is the background radially dependent density field, $\tilde{g}(r)$ is the corresponding radial gravitational acceleration, and $\rho'(r, \theta)$ is the density anomaly related to the zonal flow. Expanding to higher-order balances beyond thermal wind, including the contributions due to oblateness, is possible, but it has been shown that for determination of the deep flows, thermal wind balance (Equation (1)) is the leading-order balance and is sufficient (Galanti et al. 2017c).

The zonal gravitational harmonics, induced by the dynamics, are calculated by integrating the density anomaly ρ' from Equation (1) (Kaspi et al. 2010). They are represented by

$$\Delta J_n^{\mathrm{mod}} = -\frac{2\pi}{MR_J^n}\int_0^{R_J} r^{n+2}dr\int_{s=-1}^{1} P_n(s)\rho'(r, s)ds, \tag{2}$$

where $\Delta J_n^{\mathrm{mod}}$, $n = 2, \ldots, N$ are the harmonic gravity coefficients induced by the zonal flows, M and R_J are Jupiter's mass and radius, respectively, P_n are the associated Legendre polynomials, and $s = r\sin(\theta)$. The gravity harmonics can be used to calculate the latitude-dependent gravity anomalies in the radial direction $\Delta g_r^{\mathrm{mod}}(\theta)$, so representation of the model results is available in both terms (Kaspi et al. 2010; Galanti et al. 2017b).

Giant planets are, to leading order, north–south symmetric bodies. The value of the low-degree even gravity harmonics reflect mostly the internal mass distribution within the planet, resulting from the planet's shape and rotation (Hubbard 2012). Therefore, the even degrees ($n = 2, 4, 6 \ldots$) resulting from the flow are difficult to differentiate from the total values and might not be a good indicator for the dynamics (Kaspi 2013; Kaspi et al. 2017). If no north–south asymmetry exists, the odd J_n should be identically zero. *Juno* was able to measure all of the gravity harmonics within the sensibility range (Iess et al. 2018), and found significant non-zero values for the odd gravity harmonics. Since rigid body rotation cannot explain these values, wind asymmetry between the hemispheres must be the cause for the odd J_n. Consequently, for the odd harmonics $\Delta J_n = J_n$. Following Kaspi et al. (2018), we use the TW approach to calculate the flow decay profile that can explain the four odd gravitational moments (J_3, J_5, J_7, and J_9) within the uncertainty range. Unlike Kaspi et al. (2018), we also require that this profile is physically consistent with magnetic field considerations as described below.

2.2. Time-dependent Magnetic Field Constraints

The temporal variation of Jupiter's magnetic field can be described by the Maxwell equations, combined to set the EM induction equation (e.g., Jones et al. 2011),

$$\frac{\partial \boldsymbol{B}}{\partial t} = \nabla \times (\boldsymbol{u} \times \boldsymbol{B}) - \nabla \times (\eta \nabla \times \boldsymbol{B}), \tag{3}$$

where $\boldsymbol{B}$ is the three-dimensional magnetic field, $\boldsymbol{u}$ is the three-dimensional velocity, and $\eta = \frac{1}{\mu_0 \sigma}$ is the magnetic diffusivity with μ_0 being the magnetic permeability of free space, and $\sigma(r)$ is the electrical conductivity.

If Jupiter's internal flow indeed extends down to regions of high electrical conductivity, a non-negligible effect on the time-dependent magnetic field is expected. This effect is not the only one that can cause magnetic secular variation, and other effects such as an external magnetodisk (Ridley & Holme 2016), internal dynamo variabilities (Jones 2014; Dietrich & Jones 2018), or other rotation periods (Moore et al. 2019) are possible. However, within the timescales that we are addressing, zonal flow advection is the predominant one. When only steady zonal flows are considered, the nonlinear interaction term between the flow field and the magnetic field in the radial direction becomes

$$-\frac{u}{r\sin\theta}\frac{\partial B_r}{\partial \phi}, \tag{4}$$

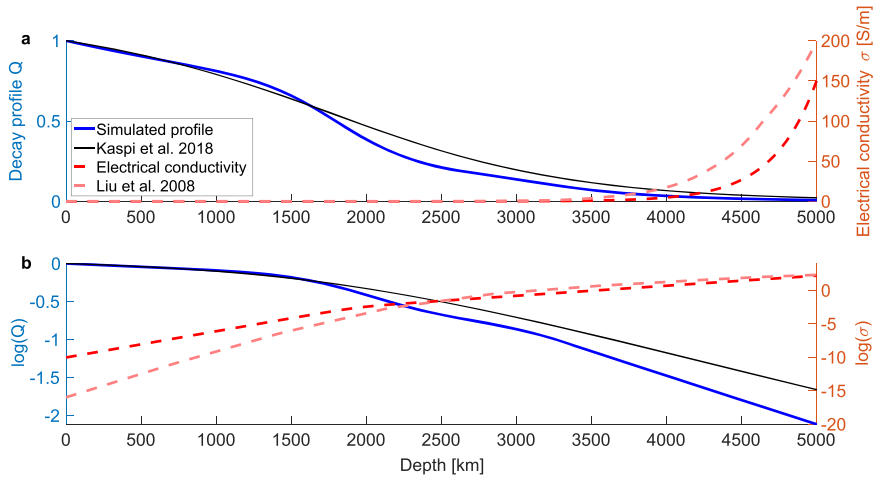

Figure 1. Decay profile of Kaspi et al. (2018; black), the simulated decay profile used to generate the $\frac{\partial B}{\partial t}$ measurements (blue), the electrical conductivity (dashed red), and the electrical conductivity as appears in Liu et al. (2008; light dashed red) in linear (a) and log scales (b).

where ϕ is longitude, θ here is co-latitude, and $\frac{u}{r\sin(\theta)}$ is the angular velocity associated with the zonal flows. The magnetic field can be decomposed into poloidal and toroidal components such that

$$\boldsymbol{B} = \nabla \times (\nabla \times P\boldsymbol{e_r}) + \nabla \times T\boldsymbol{e_r}, \tag{5}$$

where P and T are the poloidal and toroidal potentials, respectively.

Similar to the gravity decomposition, the EM induction equation is solved with a pseudo-spectral method. Using spherical harmonics in the horizontal directions and Chebyshev polynomials in the radial direction, the poloidal potential is then

$$P = \sum_n \sum_l \sum_m P_{lmn} C_n(r) Y_l^m(\theta, \phi), \tag{6}$$

where $C_n(r)$ are the Chebyshev polynomials of degree n, $Y_l^m(\theta, \phi)$ are the spherical harmonics of degree l and order m, and P_{lmn} are the coefficients associated with each combination of the Chebyshev and spherical harmonic functions. For the toroidal potential an equivalent equation is used. Note that representation of the potentials is possible also with the Schmidt coefficients as in Connerney et al. (2018). The poloidal magnetic potential governing equation then becomes

$$\frac{l(l+1)}{r^2}\left[\left(\frac{\partial}{\partial t} + \lambda\frac{l(l+1)}{r^2}\right)C_n - \lambda C_n''\right]P_{lmn} = -\int Y_l^{m*}\frac{u}{r\sin\theta}\frac{\partial B_r}{\partial \phi}d\boldsymbol{\Omega}. \tag{7}$$

where the double prime denotes the second derivative in r, $\lambda = \frac{\eta}{\eta_{\text{bottom}}}$ is the normalized magnetic diffusivity, and $\boldsymbol{\Omega}$ is the solid angle. *Juno* was able to measure the three components of the magnetic field outside of Jupiter (the scalar potential field) in the first year of its orbit (Connerney et al. 2018), which can be used to construct a map of the averaged B_r during the first year of measurements (the *Juno* reference model through Perijove 9, JRM9). In the following orbits, *Juno* will continue to measure the scalar potential of Jupiter's magnetic field to generate a new map of the averaged B_r during this time. If there will be notable change in the spatial structure of B_r between the two periods, the induction relation can be used to determine the vertical profile of the flow. We search for a flow decay profile that will generate changes in the magnetic field (and therefore in P and T) that will best fit the measured time changes in B_r.

2.3. Simulation and Measurements

Gravity measurements are already available (Iess et al. 2018), while the temporal variation in the magnetic field is not; therefore, validation of the solution is possible only with respect to one of the two measurements that we aim to explain. In order to test the methodology presented here, we simulate the time-varying magnetic field measurements. The simulated measurements are generated by integrating the induction equation (Equation (3)) with a chosen flow structure ($\boldsymbol{u}$ in Equation (3)) for approximately one year.

Using the decay profile of Kaspi et al. (2018) is found to be inconsistent with the time-varying magnetic field. The resulting time variation in the magnetic field, after integrating the induction model for one year, is too large and not physical (not shown). This by itself indicates that the Kaspi et al. (2018) profile is too strong in regions of high electrical conductivity and hence cannot be used to constrain the flow at depths below ~3000 km. Moreover, any solution that includes substantial deeper zonal flows will be inconsistent with the magnetic field constraints (e.g., Kong et al. 2018).

Therefore, we define a modified decay profile that is similar to the Kaspi et al. (2018) profile above ~2000 km and weaker below (Figure 1), yet still generates reasonable gravity harmonics (Table 1). The induction model is then integrated with the new profile to create "measurements" of the time-varying magnetic field according to Equations (3)–(7). We set this decay profile with a relatively small number of parameters, but with enough freedom to contain the needed complexity. The upper region is similar to Kaspi et al. (2018), and the lower region is a simple exponential decay, so that the overall

Table 1
The Odd Gravity Harmonics from *Juno*, the Kaspi et al. (2018) Model Results, the Simulated Profile, and the New Combined Model Results

Harmonic	Measured	Kaspi et al. (2018)	Simulation	Model Solution
$J_3(\times 10^{-8})$	-4.24 ± 0.91	-5.71 ± 1.67	-1.72	-4.48
$J_5(\times 10^{-8})$	-6.89 ± 0.81	-7.73 ± 0.41	-7.61	-7.69
$J_7(\times 10^{-8})$	12.39 ± 1.68	12.77 ± 0.54	10.87	12.42
$J_9(\times 10^{-8})$	-10.58 ± 4.35	-8.84 ± 0.42	-7.11	-9.02

Note. The uncertainties are the 3σ uncertainty values for the measurements and the Kaspi et al. (2018) model.

simulated flow structure is

$$U_s(\theta, r) = U_{\text{surf}}(s) Q_s(r), \tag{8}$$

$$Q_s(r) = (1 - \alpha)\exp\left(\frac{r - R_J}{H_1}\right) + \alpha\left[\frac{\tanh\left(-\frac{R_J - H_2 - r}{\Delta H}\right) + 1}{\tanh\left(\frac{H_2}{\Delta H}\right) + 1}\right] \quad R_T \leqslant r \leqslant R_J, \tag{9}$$

$$Q_s(r) = Q_s(r = R_T)\exp\left(\frac{r - R_T}{H_3}\right) \quad r < R_T, \tag{10}$$

where $U_{\text{surf}}(s)$ is the measured wind at R_J (Tollefson et al. 2017) projected toward the planet's interior in the direction parallel to the spin axis, $Q_s(r)$ is the radial decay simulated function (Figure 1), and the set of parameters that forms the decay rate are: $\alpha = 0.5$, $H_1 = 2389$, $H_2 = 1830$ km, $\Delta H = 500$ km, $R_T = 0.958R_J$, and $H_3 = 660$ km.

Interestingly, it appears that J_3 is very sensitive to depths of 2500–4000 km and that a weak flow at those depths does not allow fitting J_3 to the *Juno* measurements. Combined with the fact that the induction model requires very weak flow below 3500 km, in order to generate reasonable changes in the magnetic field, we find that J_3 constrains the flow to reach deeper than 3500 km, but the flow at those depths cannot be higher than $\sim$5–10 m s^{-1}, and can reach no more than $\sim$1 m s^{-1} at 5000 km.

Due to Jupiter's large mass, its electrical conductivity is relatively high close to its surface. To date, Jupiter's electrical conductivity profile in the upper 5000 km of the planet is based mostly on ab initio simulations and shock wave experiments (Nellis et al. 1992, 1995; Weir et al. 1996; Liu et al. 2008; French et al. 2012). The latest published magnetic field (Connerney et al. 2018), combined with the induction model, requires relatively low conductivity at depths of 2000–5000 km, to allow reasonable changes in the magnetic field with time. The conductivity profile chosen here is similar to the profile of Cao & Stevenson (2017), and is within the error range of the Liu et al. (2008) profile (Figure 1). We model the magnetic diffusivity (the inverse of the electrical conductivity) similar to Jones (2014), Cao & Stevenson (2017), and Dietrich & Jones (2018) such that

$$\eta(r) = F \cdot \exp\left(c + \sqrt{c^2 + d}\right) \tag{11}$$

where $c = \frac{1}{2}[(g_1 + g_3)r - g_2 - g_4]$, $d = (g_1 r - g2)(g_3 r - g_4) - g_5$, $F = 10$, $g_1 = 645.81$, $g_2 = 611.42$, $g_3 = 246.03$, $g_4 = 222.54$ and $g_5 = 0.21919$.

The changes in the radial component of the magnetic field resulting from the simulated decay profile are shown in Figure 2(b), along with the measured B_r from *Juno*'s first nine orbits (Figure 2(a); Connerney et al. 2018), and the simulated flow that caused this change (Figure 2(c)). Both magnetic fields (Figures 2(a) and (b)) are constructed with only 10 degrees of freedom of the harmonic coefficients l and m, as in Connerney et al. (2018). The strongest changes in the magnetic field appear at latitudes 0–20°N and are caused due to flows that penetrate areas of high electrical conductivity (Figure 2(c)). The cylindrical projection of the surface winds, parallel to the axis of rotation, causes the strong jet at 20°N at the surface to shift equatorward and causes the strong variation in B_r at $\sim$10°N. We will next consider this time-varying magnetic field as an example for the expected *Juno* measurements.

2.4. The Combined Gravity-magnetic Optimization

The measurements of the magnetic field, given at the planet's surface, can be projected in the radial direction to the regions where the conductivity is no longer negligible (Galanti et al. 2017a), according to potential field continuation. The comparison between the model and the measurement should be at this depth, chosen here as $R_c = 0.972R_J$, as in Galanti et al. (2017a). We choose to fit the measurements with a simple exponential decay flow profile in the regions of the induction model as we expect that the strong electrical conductivity in this region will cause the flow to dissipate fast and proportionally to the electrical conductivity itself, which is also exponential. The flow in this region is modeled such that

$$U_{\text{Model}}(\theta, r) = U_{\text{surf}}(s) Q_M(r), \tag{12}$$

$$Q_M(r) = U_M \exp\left(\frac{r - 0.972R_J}{H_M}\right) \quad 0.93R_J \leqslant r \leqslant 0.972R_J, \tag{13}$$

where U_M is the flow strength at $r = 0.972R_J$ relative to the surface flow, and H_M is the exponential decay rate. The search for the best solution is made by comparing the resulting changes in the magnetic field from the model to the simulation. Each model run with different U_M and H_M, using a cost-function (scalar measure) to find the best solution. The cost-function is defined as

$$L_{\text{MSV}} = \sum_{n=1}^{10}\sum_{m=0}^{n}\left[\left(\frac{\partial g_{nm}^{\text{sim}}}{\partial t} - \frac{\partial g_{nm}^{\text{mod}}}{\partial t}\right)^2 + \left(\frac{\partial h_{nm}^{\text{sim}}}{\partial t} - \frac{\partial h_{nm}^{\text{mod}}}{\partial t}\right)^2\right] \quad 0.93R_J \leqslant r \leqslant 0.972R_J, \tag{14}$$

where g_{nm}^{sim} and h_{nm}^{sim} are the simulated harmonic Schmidt coefficients (Connerney et al. 2018) at the upper boundary of the model, and g_{nm}^{mod} and h_{nm}^{mod} are the model solution for those coefficients (not to be confused with the gravity anomaly Δg_r). We then define the model solution as the average between all the solutions of the lowest order of magnitude of the resulting cost-function.

We define the transition between the MSV model and the TW model as a distinct boundary (R_T) that needs to be set in the optimization process. For the upper region of the solution

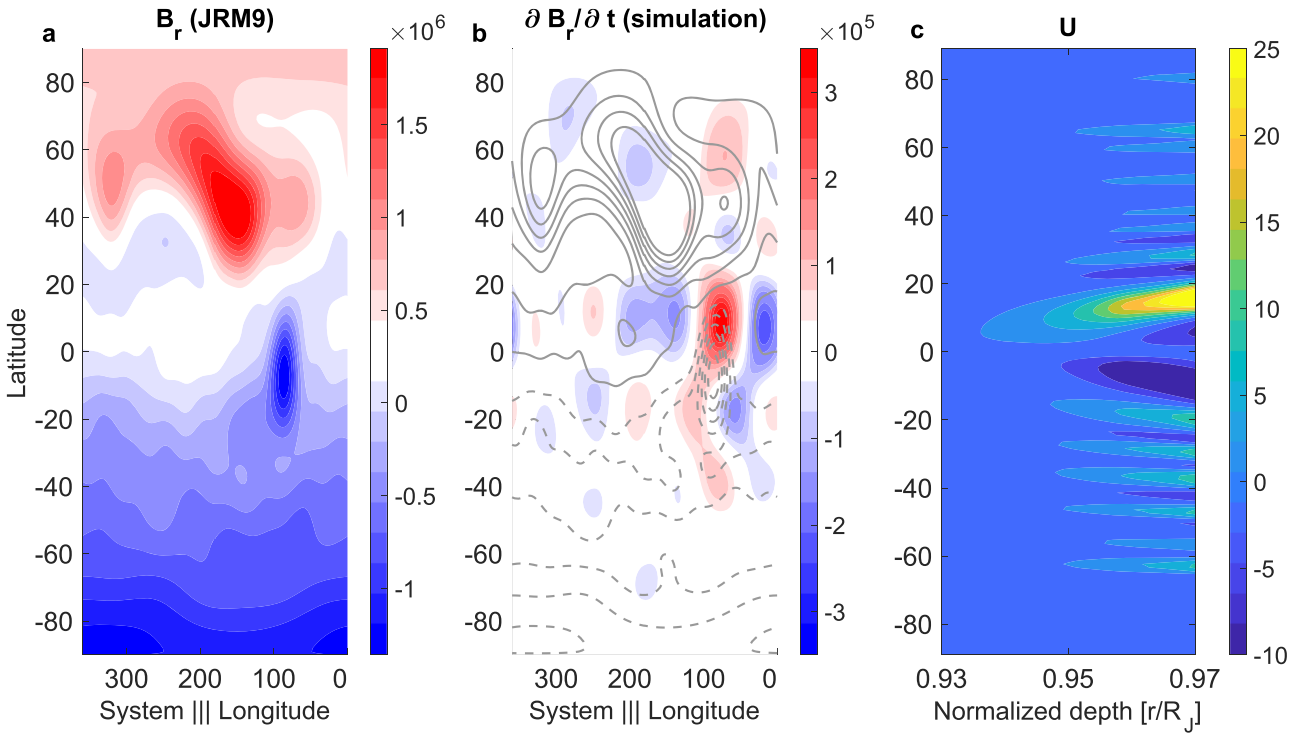

Figure 2. (a) The magnetic field [nT] measured from *Juno*'s first nine orbits (JRM9) at $\sim 0.972 R_J$ (Connerney et al. 2018). (b) The changes in the magnetic field [nT · yr^{-1}] caused by the simulated profile after 1 yr at the same depth, with gray contours showing the measured magnetic field (JRM9). (c) The simulated zonal flow as function of latitude and depth [m s^{-1}] at depths between 0.97 R_J and 0.93 R_J. Both (a) and (b) are represented here with only 10° and orders of the magnetic harmonic coefficients as in Connerney et al. (2018).

($R_T < r \leqslant R_J$), we use the TW inversion approach (Galanti & Kaspi 2016, 2017), fitting the gravity odd harmonics that resulted from the forward model to the measured ones, using a second cost-function,

$$L_{\mathrm{TW}} = \sum_{i=3,5,7,9} \sum_{j=3,5,7,9} w_{ij} (J_i^{\mathrm{obs}} - J_i^{\mathrm{mod}}) \times (J_j^{\mathrm{obs}} - J_j^{\mathrm{mod}}) \qquad R_T \leqslant r \leqslant R_J, \tag{15}$$

where J_n^{obs} are the *Juno* measurements, J_n^{mod} are the model solutions, and w_{ij} is the 4×4 weight matrix as in Kaspi et al. (2018). In the upper region, we find the best fit by optimizing the decay profile independently at each vertical grid point of the model, demanding that the vertical structure function Q is 1 at R_J and has the value of the resulted flow strength from the MSV model at the transition depth $Q_M(R_T)$. We also demand that the vertical structure function decreases monotonically with depth. The decay profile in the region between the transition depth and the upper boundary of the induction model ($R_T \leqslant r \leqslant 0.972 R_J$) is recalculated with the TW model. However, this region is still aligned with considerable conductivity, therefore we must recalculate the changes in the magnetic field to make sure that the solution is still compatible with the measurements. The value of the transition depth between the models (R_T) is determined as deeply as possible with the requirement that the time-varying magnetic field results remain valid.

3. Results

We start with the optimization of the lower region of the decay profile using the MSV model. The cost-function (Equation (14)) shows a near linear relation between the parameters U_M and H_M (Figure 3(b)). Because an optimal solution in the global minimum is not a unique point but an area (blue region in Figure 3(b)), we average the lowest order of magnitude of solutions (pink and red dots in Figure 3(b)) to determine the optimal decay rate in the inner layers (Figure 3(a), green line). The solution is obtained with $U_M = 0.6514$ and $H_M = 0.66$. The resulting model solution (green line) is very far from the simulated decay profile (black dashed line) in the region of 2000–3000 km, but converges to the simulated decay profile deeper than ~3000 km. This suggests that the transition depth (R_T, Equation (15)) should be deeper than ~3000 km ($\cong 0.958 R_J$), chosen here as $R_T =$ 3500 km ($\cong 0.95 R_J$).

Next, using the TW model, we find a solution for the decay profile that is constrained with the MSV solution at $R_T = 0.95 R_J$. The new solution fits both the *Juno* measurements and the simulation for the changes in the magnetic field (Figure 3(a), red). This combined gravity-magnetic solution shows a unique pattern of two rapid and perhaps unrelated decay patterns. The first, close to the cloud-level, might account for a baroclinic atmospheric outer layer (e.g., Kaspi & Flierl 2007) that decays until reaching a nearly barotropic state; and the second, around $H =$ 3500 km, that could reflect the magnetic braking. However, the first decay is very close to the cloud-level where neither model is sensitive (it is a non-conductive layer and the density anomalies are small), so this decay is not necessarily physically meaningful. For example, another more smoother solution, which is optimized with fewer free parameters, can be constructed (Figure 3(a), light dashed red). This solution is more similar to the Kaspi et al. (2018) solution, but its ability to explain all the odd gravity harmonics is not as good as the best-fit solution (Figure 3(a), red). The

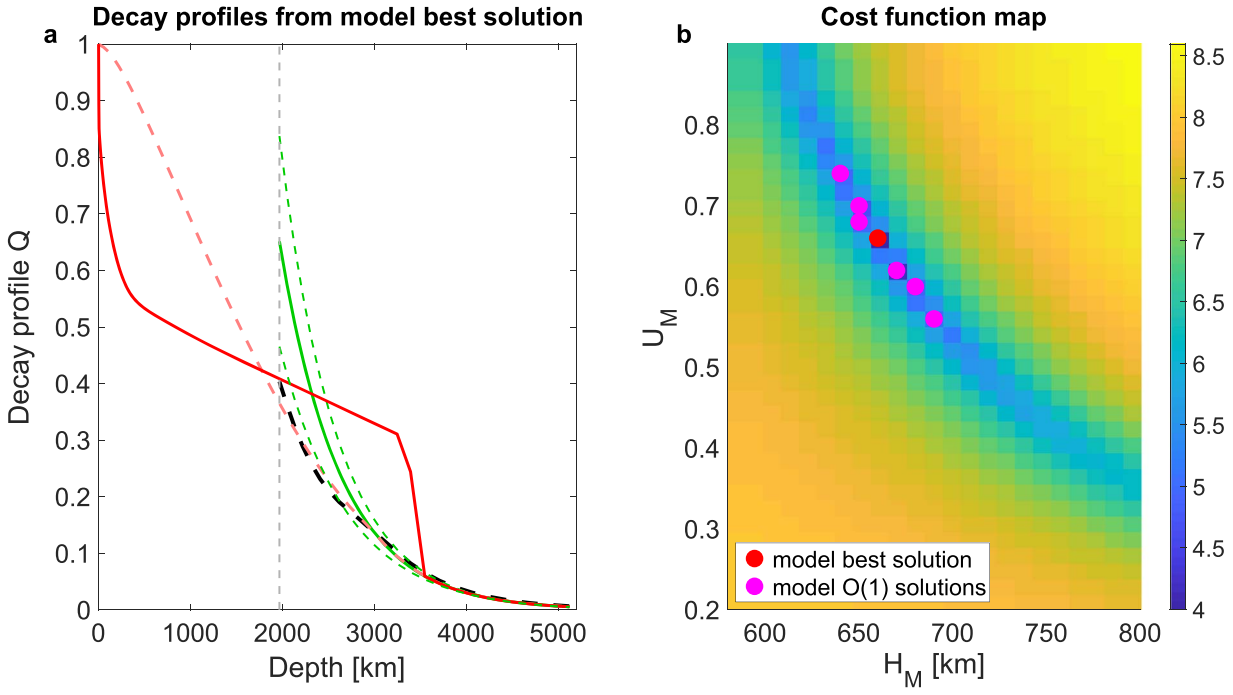

Figure 3. (a) Simulated decay profile (dashed black) together with the induction model solution for the lower region (green), its 3σ uncertainty (dashed green), the TW model solution for the upper region combining with the induction solution below R_T (red), and an additional option for the combined solution (light dashed red); also shown is the induction model boundary at 0.972 R_J (dashed gray). Note that the induction model solution is very good below ∼3000 km, in regions where the conductivity is high. (b) The cost-function map for the induction model as function of the two optimized parameters: the exponential decay rate (H_M) and the flow strength at the induction model upper boundary relative to the surface flow (U_M). Also shown are the model best solution (red and all solutions within O(1) from it (pink).

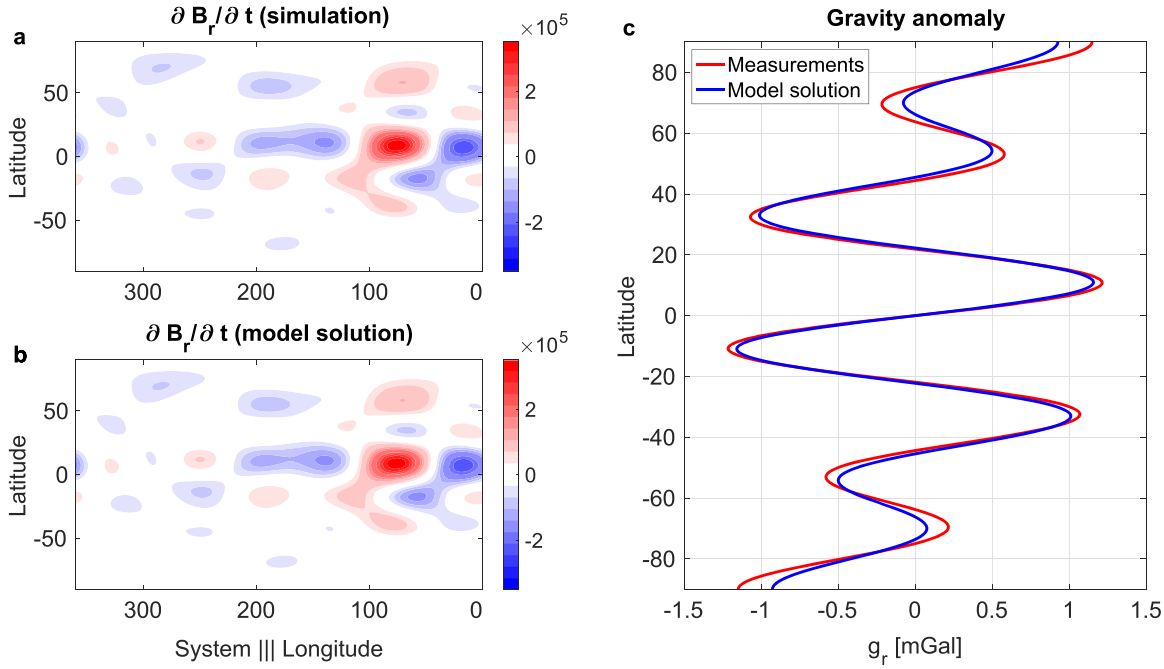

Figure 4. Combined gravity-magnetic solution. (a) The resulting time changes in B_r [nT · yr^{-1}] from the simulation, (b) the model solution for the changes in B_r [nT · yr^{-1}] after the same time span, and (c) the gravity anomalies as measured by *Juno* (red) and as calculated from the model best solution result (blue).

four odd gravitational harmonics associated with this solution are: $J_3 = -1.71$, $J_5 = -6.83$, $J_7 = 9.86$, and $J_9 = -6.54$.

To make sure that the combined best-fit solution fits also the MSV measurements, the magnetic field anomalies are recalculated from the new profile. The resulting magnetic field variation is almost identical to the variation from the MSV model solution alone. This confirms that the changes in the magnetic field are not sensitive to the flow structure above ∼3000 km (≅0.958R_J). The gravity harmonics of the resulted decay profile are displayed in Table 1 (last column), the changes in the magnetic field are shown in Figure 4(b), and the gravity anomalies in Figure 4(c) (blue). Figure 4 also shows

the simulated changes in the magnetic field (a) and the *Juno* measured gravity anomalies (c) (red).

The method presented here provides a very good solution for the measurements created by the simulated profile, but should not be taken as a solution for Jupiter's deep flows, as the magnetic field changes are based on our simulation and not the actual measurements. Once the magnetic measurements based on the following perijoves are available, the solution for the flow decay profile could be recalculated. Fitting these two independent measurements simultaneously will help to better constrain Jupiter's deep flow structure.

4. Conclusions

So far, the *Juno* gravity measurements showed that cloud-level winds extend to a depth of about 3000 km (Kaspi et al. 2018). As the gravity field is mostly sensitive to density anomalies (and hence to flow strength) at depths of no more than a few thousand kilometers, it is not possible to strongly constrain the strength of the flow below that as the flow there is weak. Measurements of the time-varying magnetic field of Jupiter might help to tackle this problem.

Here, we present a new combined method that uses two independent measurements from *Juno* to better resolve Jupiter's internal flow structure. We use the thermal wind balance that relates the flow structure to the asymmetric gravity field, and the electromagnetic induction equation that explains changes in the measured magnetic field caused by the deep flow. Because the time-varying magnetic field measurements are not yet available, we use the current gravity measurements and simulate changes in the magnetic field to find a decay profile that fits both. We find that the flow decay profile of Kaspi et al. (2018) is too strong at depths of more than $\sim$3000 km and that further constraints must be added in order to fit both measured fields. We show that a decay profile that fits both the gravity measurements and the simulated magnetic measurements can be found through a joint optimization. Once the new magnetic measurements will be available we can reoptimize the solution to find a better flow structure.

We also find that J_3 is very sensitive to the deeper regions of the atmosphere while the MSV method limits the same region to low velocities, therefore posing upper and lower bounds for the flow velocity in the deep regions. The MSV method further constrains the deepest regions of the model such that strong flows cannot exist at all below $\sim$4000 km, and nearly no flow (less than 1 m s^{-1}) can exist below $\sim$5000 km. Finally, we find that the best solution is characterized with two rapid decays instead of one as in Kaspi et al. (2018), which could represent two distinct decay mechanisms for the flow, each at a different depth range.

We thank H. Cao for providing the MSV model and for the very helpful discussions and suggestions. We also thank J.E.P. Connerney, J. Bloxham, and R. Holme for very useful comments. This research has been supported by the Israeli Space Agency and the Helen Kimmel Center for Planetary Science at the Weizmann Institute of Science.

ORCID iDs

Keren Duer https://orcid.org/0000-0003-4428-2700
Eli Galanti https://orcid.org/0000-0002-5440-8779
Yohai Kaspi https://orcid.org/0000-0003-4089-0020

References

Bloxham, J. 1992, JGRB, 97, 19565
Bloxham, J., & Gubbins, D. 1985, Natur, 317, 777
Cao, H., & Stevenson, D. J. 2017, Icar, 296, 59
Connerney, J. E. P., Kotsiaros, S., Oliversen, R. J., et al. 2018, GeoRL, 45, 2590
Dietrich, W., & Jones, C. A. 2018, Icar, 305, 15
French, M., Becker, A., Lorenzen, W., et al. 2012, ApJS, 202, 5
Galanti, E., Cao, H., & Kaspi, Y. 2017a, GeoRL, 44, 8173
Galanti, E., Durante, D., Finocchiaro, S., Iess, L., & Kaspi, Y. 2017b, AJ, 154, 2
Galanti, E., & Kaspi, Y. 2016, ApJ, 820, 91
Galanti, E., & Kaspi, Y. 2017, Icar, 286, 46
Galanti, E., Kaspi, Y., & Tziperman, E. 2017c, JFM, 810, 175
Gastine, T., & Wicht, J. 2012, Icar, 219, 428
Gastine, T., Wicht, J., Duarte, L. D. V., Heimpel, M., & Becker, A. 2014, GeoRL, 41, 5410
Holme, R., & Olson, P. 2007, Treatise on Geophysics, 8, 107
Hubbard, W. B. 2012, ApJL, 756, L15
Iess, L., Folkner, W. M., Durante, D., et al. 2018, Natur, 555, 220
Jones, C. A. 2014, Icar, 241, 148
Jones, C. A., Boronski, P., Brun, A. S., et al. 2011, Icar, 216, 120
Kahle, A. B., Vestine, E. H., & Ball, R. H. 1967, JGR, 72, 1095
Kaspi, Y. 2013, GeoRL, 40, 676
Kaspi, Y., & Flierl, G. R. 2007, JAtS, 64, 3177
Kaspi, Y., Flierl, G. R., & Showman, A. P. 2009, Icar, 202, 525
Kaspi, Y., Galanti, E., Helled, R., et al. 2017, GeoRL, 44, 5960
Kaspi, Y., Galanti, E., Hubbard, W. B., et al. 2018, Natur, 555, 223
Kaspi, Y., Hubbard, W. B., Showman, A. P., & Flierl, G. R. 2010, GeoRL, 37, L01204
Kong, D., Zhang, K., Schubert, G., & Anderson, J. D. 2018, PNAS, 115, 8499
Liu, J., Goldreich, P. M., & Stevenson, D. J. 2008, Icar, 196, 653
Moore, K. M., Cao, H., Bloxham, J., et al. 2019, NatAs. tmp, 325
Moore, K. M., Yadav, R. K., Kulowski, L., et al. 2018, Natur, 561, 76
Nellis, W. J., Mitchell, A. C., McCandless, P. C., Erskine, D. J., & Weir, S. T. 1992, PhRvL, 68, 2937
Nellis, W. J., Ross, M., & Holmes, N. C. 1995, Sci, 269, 1249
Ridley, V. A., & Holme, R. 2016, JGRE, 121, 309
Tollefson, J., Wong, M. H., de Pater, I., et al. 2017, Icar, 296, 163
Vallis, G. K. 2006, Atmospheric and Oceanic Fluid Dynamics (Cambridge: Cambridge Univ. Press)
Vestine, E. H., & Kahle, A. B. 1966, JGR, 71, 527
Weir, S. T., Mitchell, A. C., & Nellis, W. J. 1996, PhRvL, 76, 1860